Modeling the Performance of the Standard Cirrus Glider using Navier-Stokes CFD

Thomas Hansen
Norwegian University of Science and Technology
N-7491, NTNU Trondheim, Norway
thomas.h.hansen@ntnu.no

Abstract

The performance of the Standard Cirrus glider is simulated using a Computational Fluid Dynamics code, solving the incompressible Navier-Stokes equations for steady flow. To calculate the transitional boundary layer flow a correlation-based transition model is used. It is found that the numerical model is able to predict the performance of the Standard Cirrus well. The simulations using the transition model are found to improve the results compared to fully turbulent simulations, except for the region of the stall. The best in-flight measured glide ratio for the Standard Cirrus is 36.5 at 94.5 km/h. The simulations using the transition model predict a best glide ratio of 38.5 at 95 km/h.

Introduction

The development of modern computer tools has led to a revolution in the design and construction of high-performance gliders. Today, the aerodynamic and the structural potential of new designs can be investigated and refined using computers to produce gliders with performance and handling qualities inconceivable just a few decades ago. The JS1, ASG29 and the Diana 2 are examples of modern gliders developed by using the latest computational tools in combination with experience and experimental testing. Glide ratios above 50:1 and maximum speeds higher than 280 km/h are today normal for gliders having 15 and 18 meter of wing span. However, modern numerical tools stand in sharp contrast to the methods applied for the design of the first high-performance gliders. Some 30 years ago the tools available consisted almost entirely of analytic approximation methods, wind tunnel experiments and flight testing. The materials and the accuracy of the production methods available at the time were also limiting factors in the quest to develop high-performance gliders.

In this paper, the Standard Cirrus glider is simulated by solving the Reynolds-Averaged Navier-Stokes (RANS) equations in the commercial computational fluid dynamics (CFD) software STAR-CCM+ [1]. The main purpose of the study is to create a validated reference model for the performance of the glider in steady level flight. To predict the important boundary layer flows, the correlation-based γ–Re_θ transition model is used [2,3]. The results obtained in this work should enable future investigations regarding possible performance and handling quality enhancements for the glider. The design of new winglets, the installation of an electrical engine and research on new turbulator technology are examples of studies that could benefit from using a validated RANS model. The model of the Standard Cirrus is also intended to be a reference model for investigating and refining the results from other numerical simulation tools. The abilities and limitations of less computationally expensive tools such as lifting line methods, vortex-lattice codes, and potential flow solvers can all be evaluated better by comparing the results to a validated Navier-Stokes model.

To perform the simulations, the geometry of the specific Standard Cirrus named LN-GTH is first measured using a digitizing arm and a surface model is created. Then, the performance of the airfoil used at the outer part of the Cirrus wing is analyzed using a two dimensional mesh. The simulations are performed to investigate the accuracy of the γ–Re_θ transition model in detail. The two dimensional computations are validated by comparing the results to experimental values from the low-turbulence pressure wind tunnel at NASA Langley. Finally, the three dimensional model of the Standard Cirrus is simulated in steady level flight for velocities from 90 km/h to 160 km/h. The three dimensional CFD simulations are validated by comparing the results to flight tests performed with a Standard Cirrus at the Idaflieg summer meeting in 2011.

Fig. 1: The Standard Cirrus. Lennart Batenburg, with permission

The Standard Cirrus

The Standard Cirrus (Fig. 1) was designed by Dipl.-Ing. Klaus Holighaus at the Schempp-Hirth factory and flew for the first time in March 1969. The glider is a 15-m design without flaps and was originally built to compete in the Standard Class. The glider uses an all-moving tailplane, is equipped with air brakes on the upper surface of the wings, and can carry 80 kg of water ballast to increase the flight performance. The wing of the glider is designed using two different airfoils, where the root airfoil blends linearly into the airfoil that is used

Fig. 2: Microscribe digitizing arm.

at the outer part of the wing. This outer airfoil is kept constant from the start of the aileron to the tip of the wing. The best glide ratio for the glider is about 37:1 and the maximum speed is 220 km/h. The glider is known for its good handling qualities, large cockpit and ability to climb well in turbulent thermals. Today, the Standard Cirrus is considered to be one of the best gliders for participating in club class competitions.

Method

In the following, the methods used to perform the simulations of the Standard Cirrus are presented. First, the approach used to perform the measurements of the glider geometry is explained. Then, the numerical approach used to investigate the performance of the Standard Cirrus in both two and three dimensions is given.

Measurements of the glider geometry

To perform a qualitative analysis of the flight performance for the Standard Cirrus the 'as built' geometry is measured on a specific Standard Cirrus named LN-GTH. To reproduce the glider geometry, the airfoil on both the wing, elevator and rudder is measured using a digitizing arm. The wing is measured at the root, the start of the aileron, and at the tip of the wing. Tail-section measurements are performed at the largest and smallest chord, respectively. By fixing stainless steel shims to the surface of the wing and tail at the measurement stations a straight edge is created and used to guide the digitizing arm. In Fig. 2, the digitizing arm used for the measurements is depicted. The digitizing arm is operated in combination with a surface Computer Aided Design (CAD) tool [4] and about 200 points are captured for each measurement. To increase the accuracy, five measurement series are taken for each airfoil geometry. Then, final splines of the airfoils are created in a two dimensional panel code [5] using the averaged measured data. The chord lengths of the wing and tail at the chosen stations are also measured using a 1-m digital caliper gauge. All other measurements of the glider, such as the position of the wing to fuselage fairing, height of the tail, etc., are taken using a handheld laser. Factory drawings are used as reference. The fuselage, however, is defined by modifying a CAD model which has been used to perform a similar CFD simulation of the Standard Cirrus using the TAU code at the German Aerospace Center (DLR) [6].

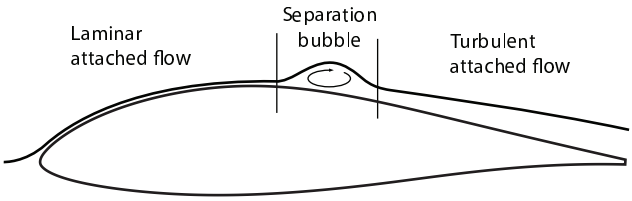

Fig. 3: Laminar separation bubble.

Navier Stokes solver

The simulations of the Standard Cirrus are performed using the parallelized flow solver STAR-CCM+. The program is designed to take on all aspects of the CFD process, and tools enabling both CAD design and post-processing of the results are implemented. The meshing technology is automated and is capable of creating both a tetrahedral, polyhedral and trimmed hexahedral mesh in a Cartesian coordinate system. A wide range of turbulence models is available, including the k–ω SST turbulence model of Menter [7] which is a prerequisite for applying the γ–Re_θ transition model [1]. To solve the RANS equation for the simulations of the Standard Cirrus, the segregated solver in STAR-CCM+ is used. The flow field is modeled using a constant density model and the air is considered to be steady and incompressible. The turbulent flow is modeled with the k–ω SST turbulence model, and the transition locations are predicted using the γ–Re_θ transition model. All simulations are performed on a Dell power blade cluster running 36 CPUs in parallel.

The γ–Re_θ transition model

The laminar-turbulent transition process is important when predicting the performance of gliders. For Reynolds numbers below 3 million, this transition process often takes the form of a laminar separation bubble. When this occurs, the separating laminar layer is followed by turbulent reattachment, just behind a recirculation region. In Fig. 3 an illustration of the transition process on the upper side of an airfoil is shown. The γ–Re_θ transition model used in this study is a correlation-based transition model that solves two extra transport equations, one for intermittency, γ, and one for the local transition onset momentum thickness Reynolds number, Re_{θ_t}. The model relates the local momentum thickness Reynolds number, Re_θ, to the critical value, Re_{θ_c}, and switches on the intermittency production when Re_θ is larger than the local critical value. The only input the model requires is the definition of the location for the free-stream edge. This means that a distance from the wall of the geometry has to be estimated to ensure that the entire boundary layer is captured [1]. A high-quality, refined, low-Reynolds number mesh is required for using the γ–Re_θ transition model. One important parameter defining the mesh quality is the distance from the wall boundary to the first cell centroid in the mesh. This distance determines how the boundary layer is resolved by the turbulence model, and is defined by the y^+ value

$$y^+ = \frac{yu^*}{\nu} \tag{1}$$

where y is the normal distance from the wall to the first cell-centroid, u^* is the frictional velocity at the nearest wall and ν is the kinematic viscosity. To enable the γ–Re_θ transition model to converge, the y^+ values need to be in the region 0.1 to 1, and the growth rate and stream-wise

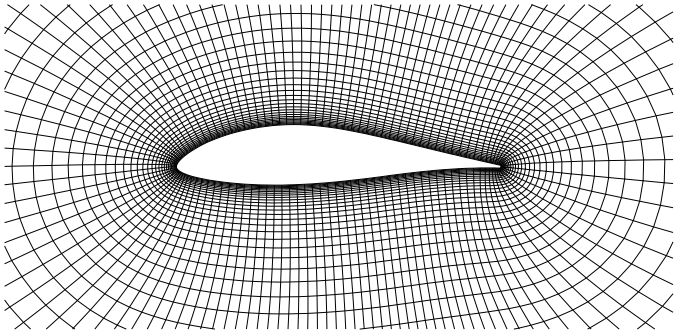

Fig. 4: Hyperbolic extruded O-mesh.

mesh spacing in the transition area needs to be fine enough to capture the laminar separation bubble [3]. By performing the simulations as fully turbulent, the transition process is ignored and only turbulent airflow is present in the boundary layer.

Two dimensional calculations

To investigate the accuracy of the γ–Re_θ transition model, the performance of the airfoil used on the outer part of the Standard Cirrus wing is investigated in two dimensions. The simulations are validated by comparing the results to experimental data from the low-turbulence, pressure wind tunnel at NASA Langley [8]. The simulated airfoil geometry is obtained from the NASA experiment performed in 1977, and is believed to be from a Standard Cirrus wing. Hence, the performance of the newly refinished LN-GTH airfoil can be compared to measurements of the original airfoil geometry. The mesh quality required to obtain a mesh independent solution using the γ–Re_θ model is taken from previous work, where a mesh dependency study was performed [9]. The interesting angles of attack, α, are calculated using an O-mesh that is constructed with a hyperbolic extrusion method using a structured mesh tool [10]. To create a pressure outlet boundary the downstream far-field edge is cut at 40 and 110 degrees. Upstream, a velocity inlet boundary is used. In Fig. 4 an example of the O-mesh is shown.

To reproduce the flow condition in the test section of the NASA wind tunnel, the turbulent intensity and turbulent viscosity ratio is defined. The value for the turbulent intensity is found from [11] to be 0.02% and a turbulent viscosity ratio of 10 is used. The correct values applied to the inlet boundary are calculated using the turbulence decay laws for the k–ω SST turbulence model [1]. All simulations are performed for a Reynolds number of 1.5 million. To ensure a converged solution a drop in accuracy to the fourth decimal is used as stopping criterion for all residuals. In addition, an asymptotic stopping criterion for the monitored coefficients, C_l and C_d is used to ensure a bounded accuracy on the fifth decimal for the last 50 iterations. For all calculations the free-stream edge definition for the γ–Re_θ model is put at 25 mm from the airfoil surface. Fully turbulent simulations are also performed and used as reference to the transition model investigations. The mesh criteria for the fully turbulent simulations are taken from previous work performed on wind turbine blades [9]. The results from the two dimensional simulations are also compared to calculations performed using the panel codes XFOIL [12] and RFOIL [13]. To match the turbulence level, an Ncrit value of 12 is used in the panel codes.

Three dimensional calculations

In steady level flight the lift produced by an aircraft needs to equal the weight. For a glider this situation occurs at a steady, unaccelerated descent, where θ is the equilibrium descent glide angle. The lift force in coefficient form is given by

$$C_L = \frac{L}{q_\infty S} = \frac{mg}{q_\infty S} \tag{2}$$

and the drag coefficient is given by

$$C_D = \frac{D}{q_\infty S} \tag{3}$$

Here, m is the mass of the glider, g is the gravitational constant and S is the reference area. The dynamic pressure q_∞ is denoted

$$q_\infty = \frac{1}{2}\rho_\infty V_\infty^2 \tag{4}$$

where ρ_∞ is the density of air and V_∞ is the free-stream velocity. Since the change in Reynolds number due to difference in density at different altitudes is small, the descent glide angle θ can be found from

$$\tan(\theta) = \frac{1}{C_L/C_D} \tag{5}$$

Hence, the descent glide angle θ is only a function of the lift-to-drag ratio, C_L/C_D, and does not depend on altitude or wing loading. However, to achieve a given C_L/C_D at a given altitude, the glider must fly at a specific velocity V_∞ called the equilibrium glide velocity. The value of V_∞ is dependent on both altitude and wing loading [14].

To evaluate the performance of the Standard Cirrus the speed polar is calculated. The polar shows the rate of sink at different free-stream velocities and is found from

$$h = V_\infty \sin(\theta) \tag{6}$$

To validate the three dimensional simulations the speed polar is compared to flight measurements performed for the Standard Cirrus at the Idaflieg summer meeting [15]. The flight data from Idaflieg are provided as calibrated air speed (CAS) using $\rho_0 = 1.225$ kg/m^3 as reference density, and the simulations are therefore also performed using this density. The performance of the glider is investigated at flight speeds between 90 km/h and 160 km/h. These are the steady level flight speeds normally used for the glider. At lower speeds, the glider should normally be circling in thermals, and not be in steady level flight. At higher speeds than 160 km/h, the large increase in sink rate deteriorates the performance of the glider. Hence, it is not preferable to fly at these speeds except when having over-predicted the altitude needed for the final glide.

To simulate the performance of the Standard Cirrus, two CFD models are constructed and calculated. One model is created to simulate the lift and drag coefficients of the wing and fuselage, where the wing, the wing fairing and the fuselage is included. To find the correct angles of attack that produce the needed lift coefficient at the specific velocities, two simulations at different angles of attack are performed. The expected linearity of the lift slope is then used to find the angle of attack that produces the required lift for the glider. To calculate the drag coefficient of the tail section another model is created. This model is constructed with both the fuselage and the tail section present, and has the elevator positioned at zero degrees angle of attack. To account for Reynolds

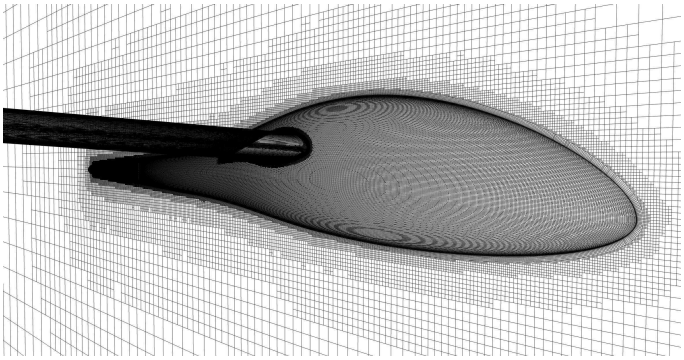

Fig. 5: Trimmed hexahedral mesh.

number effects, the drag coefficient of the tail section is simulated for all investigated velocities.

The discretization of the two models is created using an isotropic, trimmed hexahedral mesh in STAR-CCM+. To reduce the number of cells in the mesh, symmetry conditions are applied. Hence, only half the glider is present in the models. The required quality for the three dimensional grids when using the γ–Re$_\theta$ transition model is investigated for the different flight conditions. To capture the boundary layer flows, a 20-layer, 30-mm thick body-fitted hyperbolic extruded prism layer is created from the surface of the glider. The mesh outside the prism layer has a growth rate of 1.1. In Figure 5, the wing and fuselage mesh is shown. The outer boundary of the flow domain is constructed as a half-sphere, and is positioned 50 m from the glider surface. The domain is split and has a velocity inlet and pressure outlet boundary upstream and downstream of the glider, respectively. A turbulence intensity of 0.1% and a turbulent viscosity ratio of 10, initiated at the inlet boundary, is applied to specify the turbulence in the air-flow for all simulations. Convergence is assumed to be reached when a drop in accuracy to the third decimal is obtained. In addition, an asymptotic criterion is used to ensure that the monitored coefficients C_l and C_d are asymptotically bounded on the fourth decimal for the last 50 iterations. The free-stream edge definition for the simulations with the γ–Re$_\theta$ model activated is set to 50 mm. Fully turbulent simulations are also performed and the results are compared to the transition model predictions. To better investigate the difference between the two CFD methods the mesh used for the fully turbulent simulations is the same as for the calculations performed with the γ–Re$_\theta$ transition model.

Results

In the following, the results from the investigations of the Standard Cirrus glider are presented. First, the measurement of the airfoil geometry from the outer wing of the LN-GTH glider is shown and compared to the original coordinates. Then the results for the two and three dimensional simulations are given.

Geometry measurement results

The airfoil used at the outer part of the Standard Cirrus wing is found in [16] to be the FX 66-17 A II-182. This airfoil was designed by Dr. F.X. Wortmann at the University of Stuttgart and the original coordinates are obtained from the Stuttgart airfoil catalogue [17]. To investigate the quality of the airfoil on LN-GTH, comparison to both the original airfoil coordinates and to the measurements obtained from the NASA experiment are performed. In Fig. 6, the airfoil comparison is

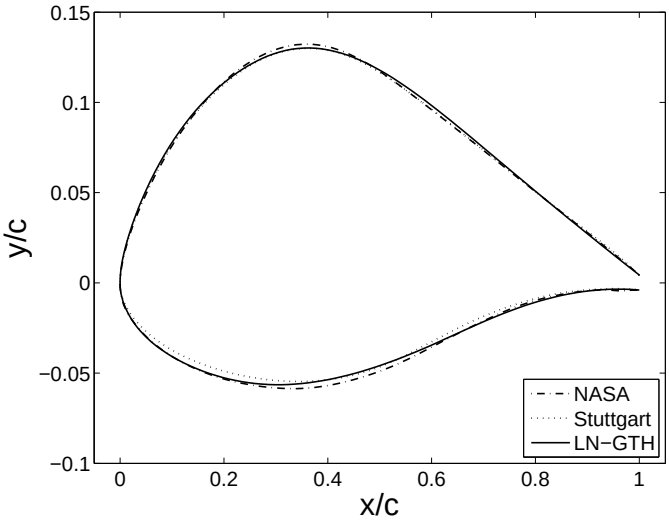

Fig. 6: Comparison of FX 66-17 A II-182 airfoils.

shown. The figure is scaled to better visualize the differences between the airfoils. As seen in the figure, the three airfoils do not match exactly. The difference between the original Stuttgart coordinates and the NASA measurements are discussed in [8] and is believed to be due to the fiberglass construction techniques available at the time of production. The airfoil geometry from the LN-GTH measurements can be seen to fit the NASA airfoil better than the Stuttgart coordinates. The largest difference between the LN-GTH and the NASA airfoil is found at the thickest part of the airfoil geometry. This difference is believed to be caused by refinishing the gelcoat on the 34-year-old LN-GTH glider.

Two dimensional results

The O-mesh with the smallest number of cells that enables the γ–Re$_\theta$ model to converge for all investigated angles of attack is taken from a mesh dependency study performed in previous work [9]. This mesh has 600 cells wrapped around the airfoil, a growth rate of 1.05 and y^+ values below 1 for all simulated angles of attack. By reducing the number of cells on the airfoil it is found that the range of angles of attack possible to simulate is also reduced. In Fig. 7, the results for the lift and drag coefficient from the two dimensional investigations are given. The top figure shows the lift coefficient versus the angle of attack. Here, the predictions from the CFD simulations using the transition model can be seen to compare well to the experimental data. The results using the transition model predict the lift coefficient equally well as the panel codes XFOIL and RFOIL for the angles of attack between -5 and $+5$ degrees. For higher angles of attack the transition model compares better to the experimental data than to the results from the panel codes. However, the transition model is unable to simulate the occurrence of the stall and the lift coefficient is over-predicted in this region. The fully turbulent CFD model can be seen to underestimate the lift coefficient for all positive angles of attack. Interestingly, the RFOIL calculations can be seen to capture the occurrence of the stall better than the XFOIL simulations. The bottom figure shows the lift coefficient C_l versus the drag coefficient C_d. Here, the predictions from the CFD simulations using the transition model can be seen to compare well to the experimental data. The transition model performs equally well as the panel codes for predicting the drag coefficient at C_l values from zero

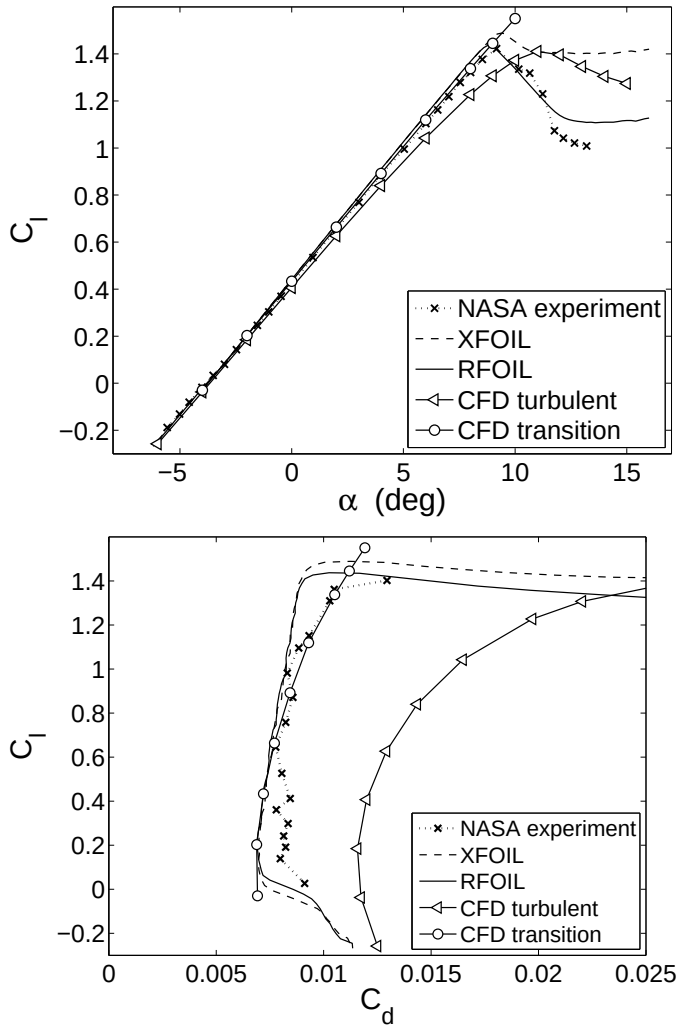

Fig. 7: Comparison of lift coefficient versus angle of attack (top) and versus drag coefficient (bottom), respectively.

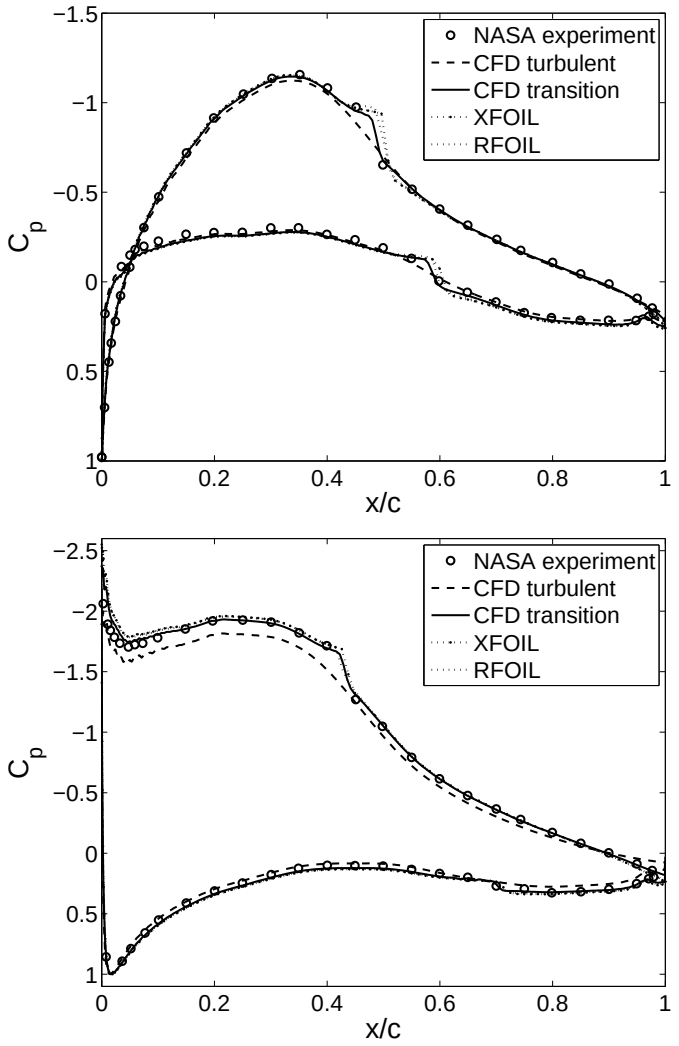

Fig. 8: Pressure coefficient distribution comparison, $\alpha = 0$ degrees (top) and $\alpha = 8.05$ degrees (bottom).

to 0.6. For higher C_l values, the drag predictions using the transition model compares better to the experimental data than the XFOIL and RFOIL results. The fully turbulent CFD model can be seen to over-predict the drag coefficient heavily for all values of C_l.

In Fig. 8, the pressure coefficient for the airfoil at angles of attack 0 and 8.05 degrees is given. By comparing the predictions from the k–ω SST model, the γ–Re_θ transition model and the XFOIL and RFOIL codes to experimental values, the performance of the different methods can be investigated in detail. In the top figure the pressure coefficients for $\alpha = 0$ degrees is depicted. At this low angle of attack only a small difference in pressure can be observed between the fully turbulent and the transition model compared to the experimental values. However, the transition model predicts the pressure slightly better on the front part of the airfoil suction side, and is also able to predict the position of the laminar separation bubbles with good accuracy. The turbulent CFD model only models the air-flow around the airfoil as turbulent and no transition is predicted. Compared to the panel codes the transition model predicts the pressure on the airfoil equally well. However, a small difference can be seen after the location of the laminar separation bubbles, which are predicted to be both larger in size and slightly further back on the airfoil for the panel codes. In the bottom figure the pressure coefficients for $\alpha = 8.05$ degrees are compared. As can be seen, the pressure on the airfoil is under-predicted using the turbulent CFD model. Specially, in the laminar region on the front part on the suction side of the airfoil the pressure is too low. It is found that by not accounting for the laminar flow present on the airfoil, this error in predicting the pressure increases for higher angles of attack. This is the reason for the lift being increasingly under-predicted at higher angles of attack in Fig. 7. The transition model, on the other hand, is able to predict the laminar air-flow in this region and the pressure compares well to the experimental data. The transition model predicts the position of the laminar separation bubbles accurately also for this flow condition. Compared to the panel codes the transition model calculates the pressure on the airfoil slightly better. The panel codes can be seen to over-predict the pressure in the region on the front part on the suction side of the airfoil. For the investigated flow conditions, the only difference between the XFOIL and the RFOIL code is the small deviation

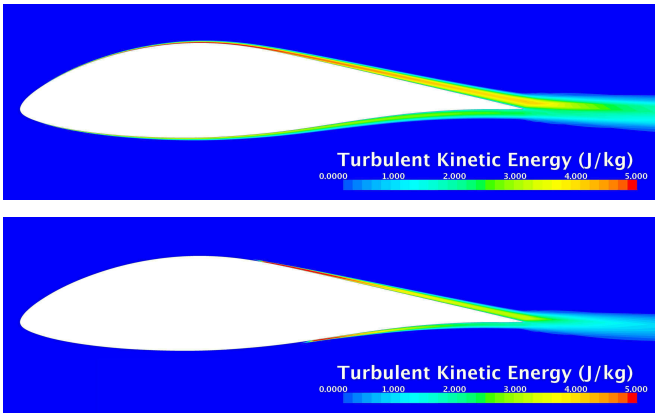

Fig. 9: Turbulent kinetic energy prediction at $\alpha = 0$ degrees for turbulent model (top) and transition model (bottom).

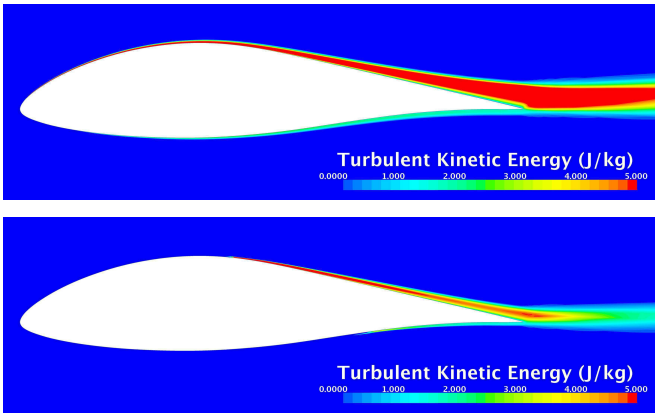

Fig. 10: Turbulent kinetic energy prediction at $\alpha = 8.05$ degrees for turbulent model (top) and transition model (bottom).

found in the transition predictions.

In Fig. 9, the difference in production of turbulent kinetic energy at zero angle of attack using the k–ω SST model and the γ–Re_θ transition model is visualized. As can be seen in the top figure, no laminar flow exists when simulating the airfoil using the fully turbulent model. The production of turbulent kinetic energy is initiated at the leading edge of the geometry and increases in size along the length of the airfoil. In the bottom figure the equivalent transition model simulation is depicted. Here, the region of laminar air-flow that exists on the front part of the airfoil is captured and the production of turbulent kinetic energy begins at the reattachment point, after the laminar separation bubble.

In Fig. 10, the production of turbulent kinetic energy at $\alpha = 8.05$ degrees is visualized. Here, the difference in production of turbulent kinetic energy between the fully turbulent (top) and the transition model (bottom) simulation is much larger compared to the zero angle of attack simulations. Hence, by performing the simulations using the fully turbulent model, the over-production of turbulent kinetic energy increases for higher angles of attack. This is the cause of the increased over-prediction in drag for high lift coefficients in Fig. 7. For the transition model simulation, the production of turbulent kinetic energy is smaller. By including the laminar flow region on the airfoil, the transition model predicts the flow condition more correctly, which enables better drag predictions.

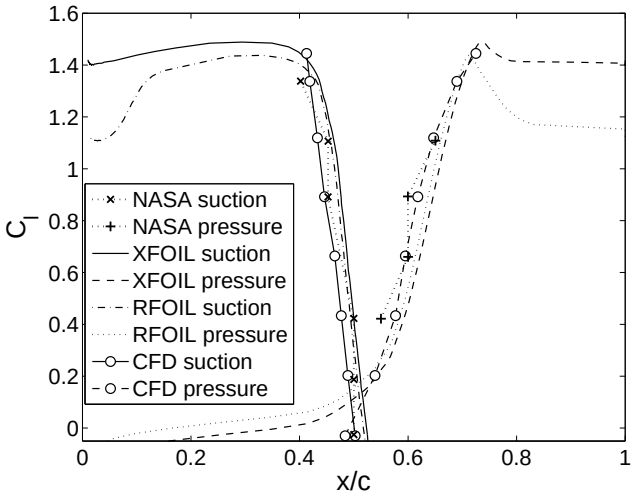

Fig. 11: Airfoil transition position.

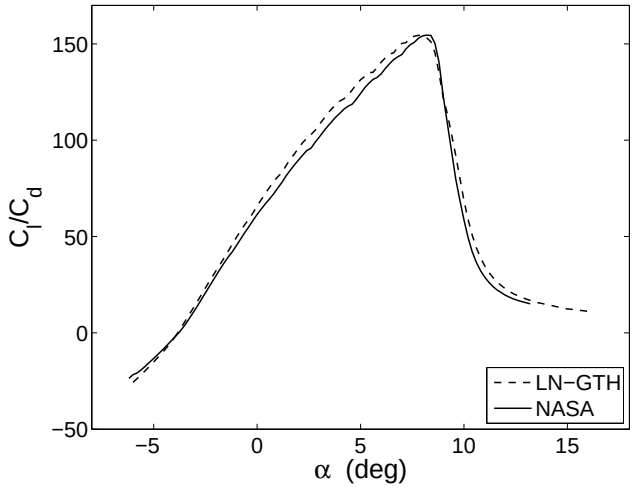

Fig. 12: Performance comparison LN-GTH and NASA airfoil.

In Fig. 11, the results for the position of the transition are given. As can be seen in the figure, the position of the laminar separation bubble using the γ–Re_θ transition model compares well to the experimental data. The prediction using the XFOIL and RFOIL codes can be seen to be slightly further back on the airfoil on both the suction and pressure side. The transition location for both the γ–Re_θ model and the panel codes are compared to the experimental data at the reattachment point where transition to turbulent flow occurs.

Finally, a comparison of the lift-to-drag ratio for the NASA airfoil measured in 1977 and the LN-GTH airfoil is depicted in Fig. 12. Here, both results are obtained using the RFOIL code and indicate a slightly better performance for the LN-GTH airfoil at angles of attack below 8 degrees for the investigated flow condition.

Three dimensional results

In Fig. 13, the constrained streamlines and the production of turbulent kinetic energy on the top side of the Standard Cirrus are visualized.

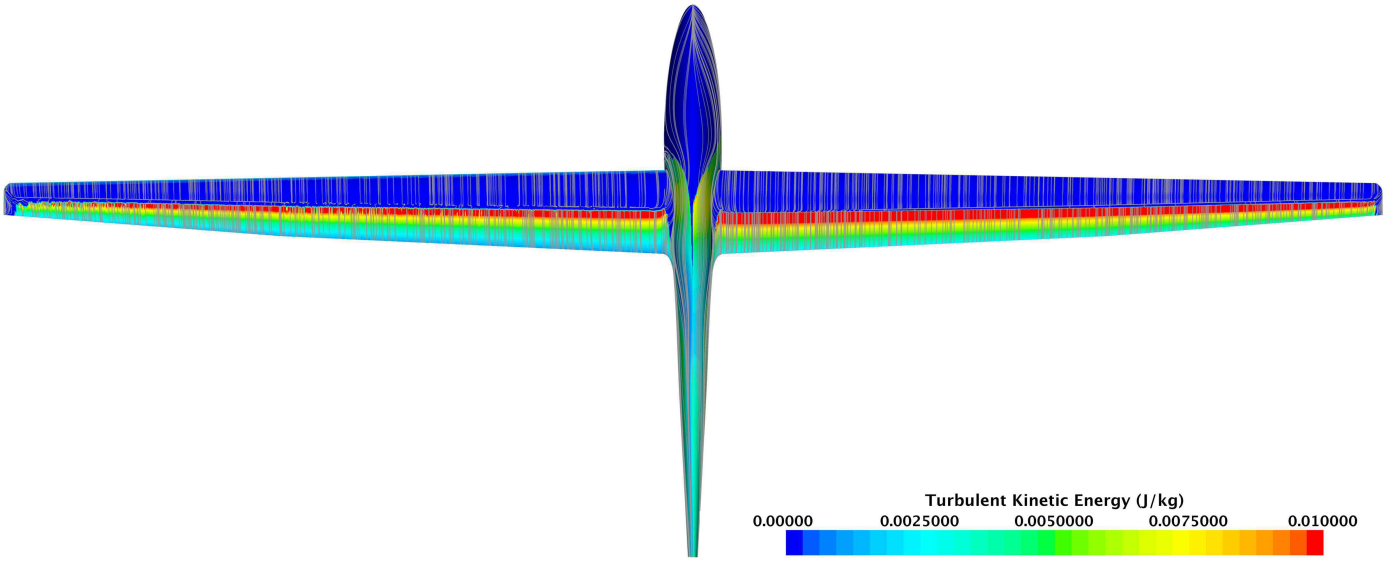

Fig. 13: Top side transition, left 95 km/h, right 160 km/h.

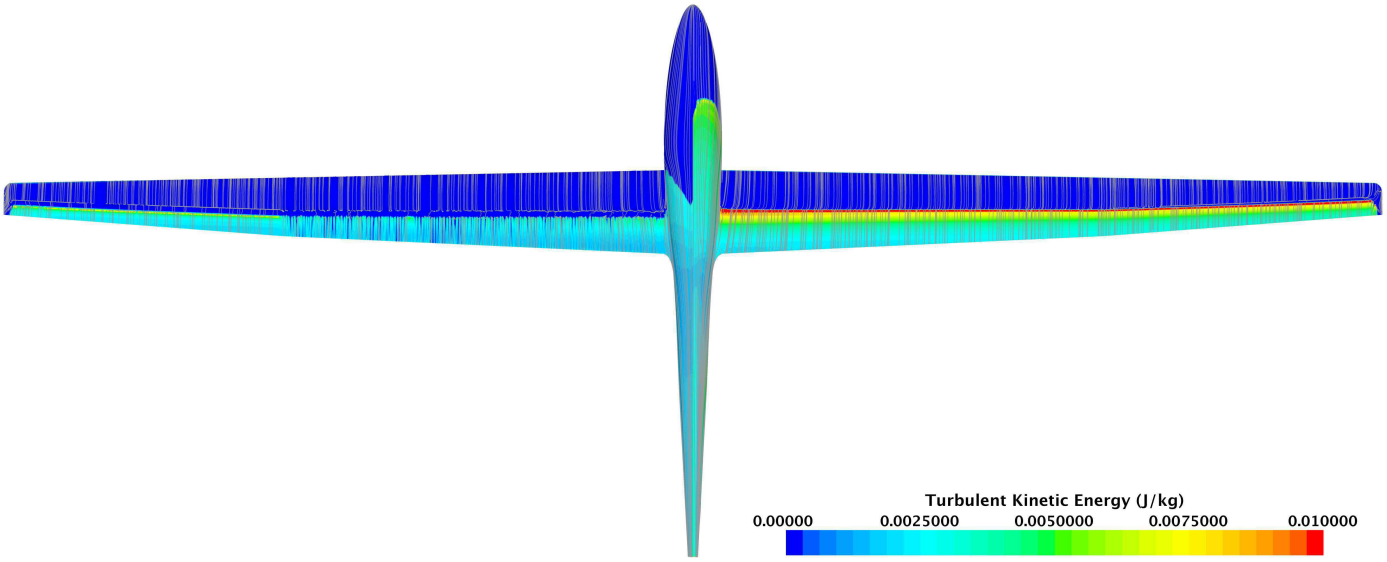

Fig. 14: Bottom side transition, left 95 km/h, right 160 km/h.

As can be seen in the figure, the transition model is able to predict both the occurrence of the laminar separation bubble and the transition from laminar to turbulent air-flow on both the wings and the fuselage of the glider. To the left in the figure a free-stream velocity of 95 km/h is applied. At this velocity the transition process starts approximately at the mid-chord along the span of the wing. The laminar separation bubble can be seen as the region where the streamlines are halted and the turbulent reattachment region, followed by turbulent attached flow is predicted by the production of turbulent kinetic energy. To the right in the figure the 160 km/h simulation is depicted. At this velocity the position of the transition is moved slightly backwards compared to the 95 km/h simulation. Due to the higher Reynolds number on the inboard part of the wing no laminar separation bubble is visible in this region and the transition process forms directly to turbulent flow. On the outer part of the wing the Reynolds number is gradually decreased and a linearly growing laminar separation bubble is formed towards the tip. The amount of turbulent kinetic energy is also increased for this flight velocity due to the increase in profile drag.

In Fig. 14, the constrained streamlines and the production of turbulent kinetic energy on the bottom side of the Standard Cirrus is shown. For the 95 km/h simulation (left in figure) the transition from laminar to turbulent flow on the bottom side starts slightly behind the mid-

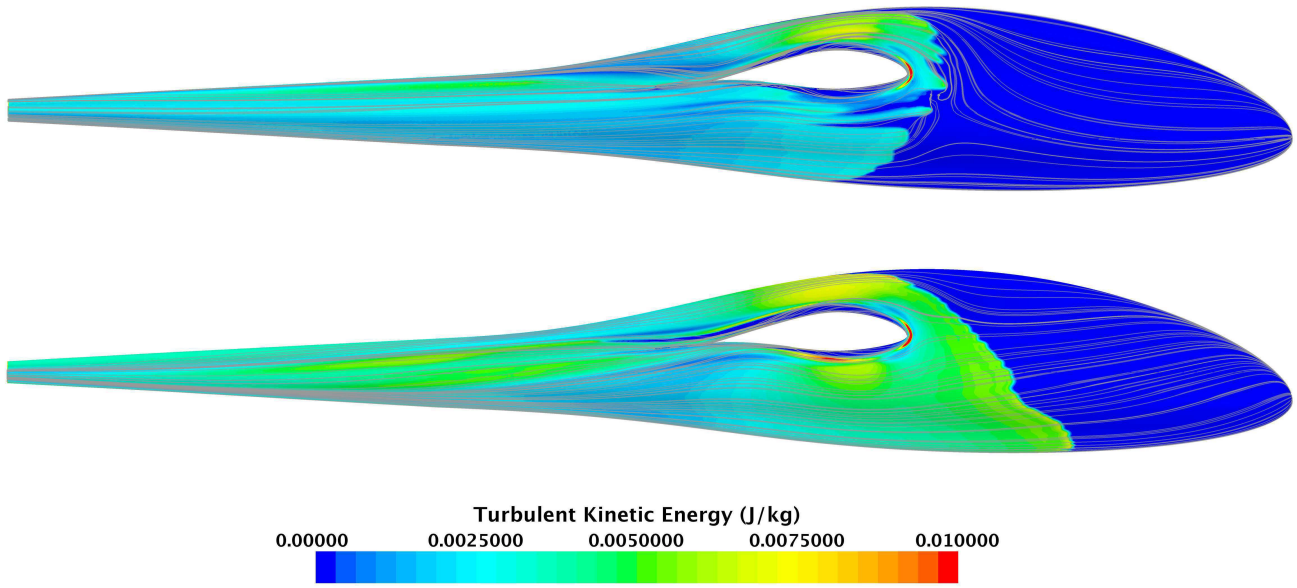

Fig. 15: Fuselage transition, top 95 km/h, bottom 160 km/h.

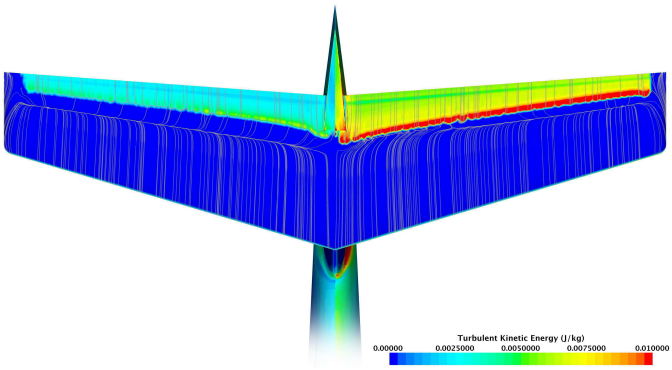

Fig. 16: Elevator transition, left 95 km/h, right 160 km/h.

chord along the span of the wing. A large laminar separation bubble is predicted and the production of turbulent kinetic energy is lower than on the suction side. For the 160 km/h simulation (right in figure) the position of the transition is moved slightly forward compared to the 95 km/h simulation. Again, most of the transition forms directly to turbulent flow, and only on the outboard part of the wing a linearly growing laminar separation bubble is predicted due to the decrease in Reynolds number. The higher profile drag compared to the 95 km/h simulation can be seen by the larger production of turbulent kinetic energy for this simulated velocity. Interestingly, the transition model predicts little production of turbulent kinetic energy in the region of the vortex at the tip of the wing for both simulated velocities.

The constrained streamlines and the production of turbulent kinetic energy on the fuselage of the Standard Cirrus is visualized in Fig. 15. In the top figure the transition position for the 95 km/h simulation is shown. Here, the transition from laminar to turbulent can be seen to occur slightly before the wing-fuselage fairing. In the bottom figure the production of turbulent kinetic energy for the 160 km/h simulation is shown. Due to the higher velocity and smaller angle of attack at this flight condition the transition has moved forward on the lower side of the fuselage. Hence, both the fuselage shape, the angle of attack and the velocity determines how the transition process develops on the fuselage. It is known that sailplane cockpit ventilation is affected by internal flow resistance within the fuselage, causing air to escape between the canopy frame and the cockpit edge. Depending on the amount of leakage this might trip the laminar boundary layer on the cockpit edge to turbulent flow and increase the profile drag for the fuselage [18]. This phenomena is not captured by the simulations performed in this work. However, the position of the boundary layer transition line for the simulations are found to compare well to measurements found in [16].

In Fig. 16, the constrained streamlines and the production of turbulent kinetic energy on the top of the elevator is shown. Again, the trends from the simulations performed on the wings of the glider can be observed. For the 95 km/h simulation, to the left in the figure, the production of turbulent kinetic energy is small and the laminar separation bubble is large. The position of the transition for the 160 km/h simulation to the right in the figure, has moved forward and the production of turbulent kinetic energy is increased due to the increase in profile drag. As for the wing at 160 km/h, the transition bubble is only present at the outer part where the Reynolds number is lower.

The constrained streamlines and the production of turbulent kinetic energy on the lower side of the elevator and the tail section is shown in Fig. 17. To the left in the figure the result from the 95 km/h simulation is depicted and to the right the 160 km/h simulation is visualized. It can be seen that the presence of the fuselage has an impact on the production of turbulent kinetic energy on the tail section, since the turbulent flow condition from the fuselage initiates the transition process almost on

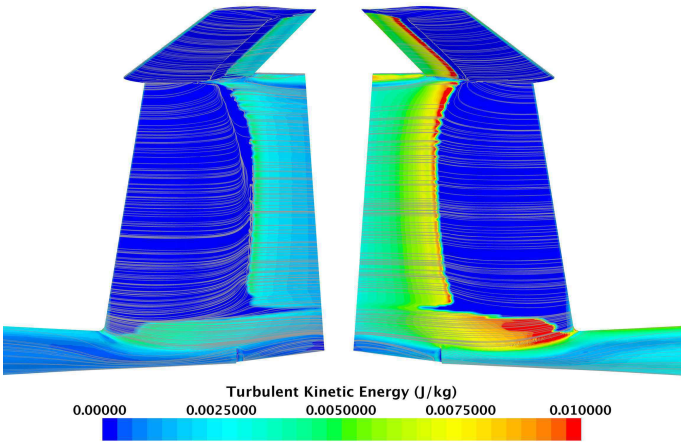

Fig. 17: Tail section transition, left 95 km/h, right 160 km/h.

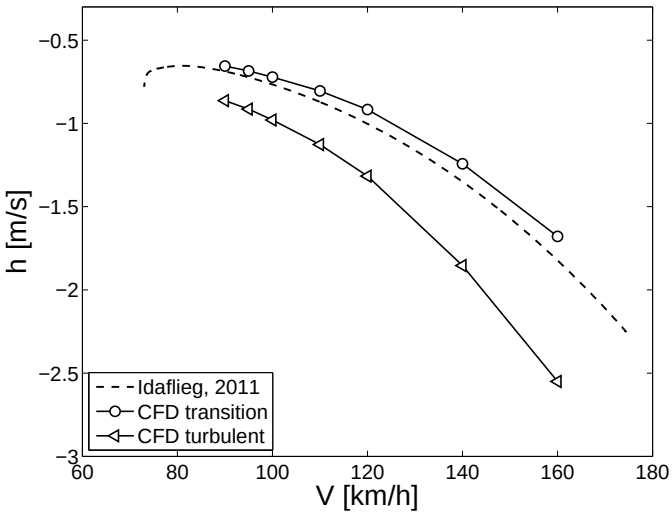

Fig. 18: Standard Cirrus speed polar comparison.

the leading edge for the lower part of the fin. Higher up on the fin the inflow condition is less turbulent and the transition occurs later. Also, in the connection between the elevator and fin more turbulent kinetic energy is produced due to increased interference drag, and the transition point is moved slightly forward. For the 95 km/h simulation a laminar separation bubble can be seen to form about half way up the fin and continues on the lower side of the elevator. For the 160 km/h simulation, however, the laminar separation bubble is only visible on the lower side of the elevator and the transition forms directly to turbulent flow on the fin section. The drag coefficient for the tail section is found to be Reynolds number dependent and a reduction in C_d of about 10% is found for the 160 km/h simulation compared to the 95 km/h simulation.

To obtain converged solutions for the simulations using the γ–Re_θ model the calculated grids are adjusted to fulfil the mesh criteria due to differences in simulated velocities and angles of attack. Since the y^+ value for the mesh scales with the velocity, the grids at high velocities are adjusted using a smaller distance to the first cell centroid. At angles of attack where the flow is less attached, more cells on the wing are also needed to obtain a converged solution. The number of cells in the mesh for the 90 km/h to the 160 km/h simulation is therefore gradually increased from 28 million to about 42 million cells, respectively. The simulations of the fuselage and tail section mesh have about 7.8 million cells.

In Fig.18, the calculated speed polar for the Standard Cirrus is compared to flight measurements from Idaflieg. The simulations performed using the γ–Re_θ transition model can be seen to compare well to the real flight data. For velocities below 100 km/h the simulations are closely matched to the in-flight measurements. At higher velocities, the sink rates are slightly under-predicted. The measured best glide ratio for the Standard Cirrus from the Idaflieg flight tests is found to be 36.51 at 94.47 km/h. The best glide ratio for the simulations performed using the γ–Re_θ model is found to be 38.51 at 95 km/h. The turbulent calculations of the Standard Cirrus can be seen to heavily over-estimate the drag and consequently the sink rates for all investigated velocities. The difference between the simulated results and the flight measurements also increase at higher flight speeds. This is because the friction drag on the glider is increasingly over-predicted since no laminar flow is present in the model. The best glide ratio for the fully turbulent simulations is found to be 28.96 at 90 km/h.

In Table 1 the angles of attack for the Standard Cirrus simulations are given. The zero angle of attack position for the CFD models of the glider is referenced to the weighing position as found in the flight and service manual [19]. As can be seen in the table, higher angles of attack are required to sustain steady level flight when performing the simulations as fully turbulent compared to using the γ–Re_θ transition model.

Conclusions

In this study the performance of the Standard Cirrus glider is simulated using the computational fluid dynamics code STAR-CCM+. The turbulent flow is modelled using the k–ω SST turbulence model and the transition locations are automatically predicted using the γ–Re_θ transition model. To investigate the performance of the γ–Re_θ model, calculations on a Cirrus airfoil are first performed using a two dimensional grid. The final three dimensional simulations of the glider are validated by comparing the results to recent flight measurements from Idaflieg. It is found that the numerical model is able to predict the performance of

Table 1: Input data for CFD simulations.

V_∞	$[km/h]$	90	95	100	110	120	140	160
C_L	[-]	0.911	0.818	0.738	0.610	0.512	0.376	0.288
$\alpha_{transition}$	[deg]	2.663	1.770	1.013	-0.207	-1.128	-2.396	-3.220
$\alpha_{turbulent}$	[deg]	3.265	2.274	1.472	0.169	-0.805	-2.133	-2.992

the glider well. For low angles of attack, the γ–Re_θ transition model improves the results for the lift and drag prediction of the glider compared to fully turbulent calculations. For high angles of attack the γ–Re_θ transition model is unable to converge. The best glide ratio for the Standard Cirrus from the flight tests is measured to be 36.51 at 94.47 km/h. For the simulation using the γ–Re_θ transition model the best glide ratio is calculated to be 38.51 at 95 km/h. For the fully turbulent simulations the best glide ratio is predicted to be 28.96 at 90 km/h. The large deviations in the prediction of the performance when using fully turbulent simulations are due to the absence of laminar flow in the boundary layer of the glider.

By accounting for the drag due to air leakage from the cockpit edges, as well as the drag from the tail-skid and wing tip skids, the results from the simulations using the γ–Re_θ transition model could be further improved. In particular, the drag of the tail in this work is simulated using a simplified model where the elevator is positioned at zero angle of attack. By accounting for the extra induced drag due to the elevator deflection needed to sustain steady level flight, the results should be improved. Future studies should investigate the drag production from the glider in more detail and focus on applying the γ–Re_θ transition model for high angles of attack.

Acknowledgments

The author wishes to thank Dipl.-Ing. Falk Pätzold at the Technische Universität Braunschweig for providing the experimental data from the Standard Cirrus flight tests. Also, thanks to Ing. Bernt H. Hembre and Graeme Naismith for their help with measuring the glider geometry and to Dr. Gloria Stenfelt for her support throughout this study.

References

[1] CD-Adapco, *Introducing STAR-CCM+*, 2014, User guide, STAR-CCM+ version 9.02.

[2] Langtry, R. B. and Menter, F. R., "Correlation-based transition modeling for unstructured parallelized computational fluid dynamics codes," *AIAA Journal*, Vol. 47, No. 12, 2009, pp. 2894–2906.

[3] Malan, P., Suluksna, K., and Juntasaro, E., "Calibrating the γ–Re_θ transition model for commercial CFD," *47th AIAA Aerospace Sciences Meeting including The New Horizons Forum and Aerospace Exposition*, January 2009.

[4] Robert McNeel and Associates, *Rhinoceros NURBS modeling for Windows*, 1993–2008, User's Guide, Version 4.0.

[5] "XFLR5. Analysis of foils and wings operating at low Reynolds numbers." February 2014, Guidelines for XFLR5 v6.03.

[6] Melber-Wilkending, S., Schrauf, G., and Rakowitz, M., "Aerodynamic analysis of flows with low Mach- and Reynolds-number under consideration and forecast of transition on the example of a glider," *14th AG STAB/DGLR Symposium*, Bremen, November 2004.

[7] Menter, F. R., "Two-equation eddy-viscosity turbulence models for engineering applications." *AIAA Journal*, Vol. 32, No. 8, 1994, pp. 1598–1605.

[8] Somers, D. M., "Experimental and theoretical low-speed aerodynamic characteristics of a Wortmann airfoil as manufactured on a fiberglass sailplane," Tech. Rep. TN 0-8324, NASA, February 1977.

[9] Hansen, T., *Wind Turbine Simulations using Navier-Stokes CFD*, Master's thesis, Royal Institute of Technology, Aeronautical and Vehicle Engineering, July 2010.

[10] Pointwise, Inc., *Pointwise, reliable CFD meshing*, 2014, User manual, version 9.02.

[11] von Doenhoff, A. E. and Abbot Jr., F. T., "The Langley two-dimensional low-turbulence pressure tunnel," Tech. Rep. TN 1283, NASA, 1947.

[12] Drela, M. and Youngren, H., "XFOIL 6.9 User Primer," Tech. rep., Massachusetts Institute of Technology, November 2001, http://web.mit.edu/drela/Public/web/xfoil/.

[13] Montgomerie, B. O. G., Brand, A. J., Bosschers, J., and van Rooij, R. P. J. O. M., "Three-dimensional effects in stall," Tech. Rep. ECN-C-96-079, NREL, TUD, June 1997.

[14] Anderson Jr., J. D., *Aircraft Perfromance and Design*, McGraw-Hill, 1999.

[15] Pätzold, F., "Preliminary Results of Flight Performance Determination of Cirrus75 D-6607 S/N 633," Tech. rep., IDAFLIEG, 2012, Preliminary results from the 2011 IDAFLIEG summer meeting.

[16] Thomas, F., *Fundamentals of Sailplane Design*, College Park Press, Silver Spring, Maryland USA, 1999.

[17] Althaus, D. and Wortmann, F. X., *Stuttgarter Profilkatalog I*, Institut für Aerodynamik und Gasdynamik, Stuttgart, 2011.

[18] Jonker, A. S., Bosman, J. J., Mathews, E. H., and Liebenberg, L., "Flow over a Glider Canopy," *The Aeronautical Journal*, Vol. 118, No. 1204, June 2014, pp. 669–682.

[19] Schempp-Hirth K. G., Kircheim-Teck, *Flight and Service Manual for the Sailplane Standard Cirrus*, 1969.